Catalysis Today 235 (2014) 112–126

Contents lists available at ScienceDirect

Catalysis Today

journal homepage: www.elsevier.com/locate/cattod

Phosphine- and ammonium-functionalized ordered mesoporous carbons as supports for cluster-derived metal nanoparticles

D. Vidick[a], A.F. Leonard[b], C. Poleunis[c], A. Delcorte[c], M. Devillers[a], S. Hermans[a,*]

[a] Institute of Condensed Matter and Nanosciences, Université catholique de Louvain, Place Louis Pasteur 1, 1348 Louvain-la-Neuve, Belgium
[b] Laboratoire de Génie chimique-Nanomatériaux, Catalyse, Electrochimie, Université de Liège, Institut de Chimie, B6a, Sart-Tilman, B-4000 Liège, Belgium
[c] Institute of Condensed Matter and Nanosciences, Université catholique de Louvain, Croix du Sud 1, 1348 Louvain-la-Neuve, Belgium

ARTICLE INFO

Article history:
Received 15 November 2013
Received in revised form 28 February 2014
Accepted 5 March 2014
Available online 2 April 2014

Keywords:
Ordered mesoporous carbon
Functionalization
Bimetallic
Nanoparticles
Cluster

ABSTRACT

An ordered mesoporous carbon (OMC) was functionalized with ammonium or chelating phosphine ligands. In both cases, the functionalization procedure started by oxidation by nitric acid treatment, followed by activation of surface carboxylic acid groups with thionyl chloride, then formation of amide bonds with diamines. The pendant amine groups were then either quaternized or further reacted with phosphine. The introduced functions were used as anchors for molecular mixed-metal clusters. These organometallic grafted species could then be thermally transformed into hetero-metallic nanoparticles (NP) embedded within the mesoporous framework. The NP/OMC nanocomposites could find application in hydrogenation heterogeneous catalysis or as electrodes in fuel cells.

1. Introduction

Porous carbons have drawn a widespread attention during the past years in various domains such as energy storage (anodes for Li-ion batteries or double-layer supercapacitors [1–3]), adsorption [4,5] and as catalysts supports [6]. The most used materials in these domains, especially as supports for catalysis, are activated carbons, obtained by pyrolysis and activation of natural species such as wood residues, olive stones or orange skin for instance [7]. This high interest is mainly due to the fact that porous carbons are stable in acidic as well as in alkaline media, they exhibit a high thermal stability and the dispersed catalytic species (noble metals for instance) can be easily recovered by burning away the carbon [8]. Nevertheless, the porosity of activated carbons is very difficult to control and is highly dependent on the raw material used for its production. In addition, they often contain mineral impurities, which could interfere in the catalytic processes, their production is energy-consuming and a high burn-off of the starting material is always present [3,9]. Moreover, activated carbons are essentially microporous, which in heterogeneous catalysis leads to diffusion limitations and even deactivation upon pore blocking by reactants or products. It is known that the length of mass transport can be reduced by about 20 times if the pore sizes increase from microporous to mesoporous. For that reason, an increased attention has arisen toward the development of synthesis pathways leading to mesoporous carbons, such as carbon xerogels and ordered mesoporous carbons (OMC) [10,11]. During the last years, lots of efforts have been devoted to the preparation of ordered mesoporous carbons, in view of their remarkable structure. Indeed, in addition to their interesting features inherent to the carbonaceous nature of the framework (hydrophobicity, thermal stability, corrosion resistance), their structure can be described as a regular stacking of mesoporous channels with a defined pore width, providing a very homogeneous environment for catalytic sites.

The first preparation of OMC was described in 1999 by Ryoo and co-workers (denoted as CMK materials) [12,13]. The strategy involved is based on a nanocasting procedure, where mesoporous silica is used as a sacrificial template. In detail, carbon polymers are formed inside the pores of the mesoporous silica, followed by pyrolysis and removal of the inorganic framework by HF treatment. This route, also called hard-templating, leads to highly ordered mesoporous carbons that are perfect inverted replica of the sacrificial silica. They can be described as a stacking of nano-rods stabilized by pillars and delimiting regular mesoporous voids in-between them. The pore sizes of the carbon thus depend on the pore wall thickness of the silica template, and can be tuned upon choosing the appropriate preparation method of the latter [14]. The preparation of ordered mesoporous carbons by hard-templating was very well reviewed by several authors [15,16]. More recently, soft-templating was proposed as an alternative strategy for the preparation of OMC.

* Corresponding author. Tel.: +32 10 47 2810; fax: +32 10 47 2330.
E-mail address: sophie.hermans@uclouvain.be (S. Hermans).

http://dx.doi.org/10.1016/j.cattod.2014.03.017
0920-5861/

In this case, the carbon framework is directly created in presence of surfactant molecules in the same manner as for the synthesis of ordered mesoporous silica [11,15,17]. Such a new route is very attractive, since there is space for more flexibility in tuning the pore sizes, the spatial regularity and the surface properties. The structure is also different since the material is made of true tubular mesopores in contrast to the stacking of carbon rods delimiting mesopores, allowing for an increased mechanical stability. Though more elegant, less expensive and less time-consuming, the major drawback of the soft-templating route is the need for a precise control over the interaction between surfactant molecules and growing carbon polymer species and the kinetics of the subsequent formation of the continuous carbon framework. For that reason, the direct syntheses reported are mostly very sensitive to pH and temperature, involve very long durations when prepared in diluted aqueous media [18] and need the evaporation of large quantities of solvents in the case of Evaporation-Induced Self-Assembly (EISA) [19]. Phase separation was also reported as an alternative, but in this case, HCl is used as a catalyst, making this route not adapted when poisoning by Cl^- ions has to be avoided, for instance in catalysis [20]. Although promising alternate preparation ways have been proposed recently [21], until now, the hard-templating route remains the most widespread in the application of OMC for energy storage or heterogeneous catalysis.

Ordered mesoporous carbons indeed serve as good starting materials for further modification with catalytically active species. The most widespread is the incorporation of metallic elements (Pd, Ir, Co, Fe, etc.), either during the preparation or via post-synthetic methods. It has been shown that the use of OMC as supports lead to high performance catalysts, due to the better dispersion of the active species and the low pore diffusion resistance [22–27]. It has to be emphasized that the nature of the groups present at the surface of the porous carbons plays a key role for their further application. This important fact has been extensively reviewed by Figueiredo very recently [9]. Porous carbons principally bear oxygenated and nitrogenated surface groups that can be active sites for catalysis, be used either for anchoring catalysts or catalysts precursors, or even serve for a further functionalization of the surface [9,15]. For this latter case, many examples refer to the functionalization with sulfonic acid groups covalently attached to the surface, to produce acidic catalysts used for instance in esterification of organic acids with ethanol or alkylation of aromatic compounds [28]. Finally, surface functionalization with molecules bearing specific functions is especially interesting for anchoring catalytically active compounds, like metal complexes or nanocluster-derived nanoparticles [29,30].

A wide variety of methodologies have been used to introduce metallic nanoparticles within mesoporous carbon frameworks. The synthesis of this type of host/guest materials can be accomplished by two different procedures: either by addition of the metal precursors during the synthesis of the OMC, or by a post-synthetic incorporation of the metal precursors, usually by impregnation. One of the systems that has attracted considerable interest is the Pt/OMC nanocomposite [31–37]. Platinum nanoparticles on mesoporous carbon find applications as sensors or in hydrogenation reactions and electrochemical oxidation of hydrogen or methanol in fuel cells. Beside Pt, other metals, such as Fe, Pd, Ni, Ru and Ag have been loaded onto OMC, introducing magnetic and/or catalytic properties [38–40]. As an alternative to post-synthesis modification, metal precursors can be introduced with or before carbon precursors at the nanocasting stage to produce carbon-based nanocomposites with metals, such as cobalt, titanium, copper, iron, and nickel [41–44]. During carbonization, metal salts or oxides are spontaneously reduced to metal nanoparticles and, though part of the particles is embedded in the walls, their surface still remains accessible. The advantage of this technique is that the pores of the OMC are not obstructed, but the post-synthesis modification still remains the most versatile and widespread route. Few examples of bimetallic nanoparticles can be found and generally concern association between platinum and ruthenium for fuel cell applications [45–48]. They are usually prepared by impregnation of porous carbon with solutions of the corresponding metal salts.

Heterometallic molecular clusters are ideal precursors for bimetallic nanoparticles of controlled composition. Most of the time, the cluster-derived catalysts are found to be more active and selective than commercial catalysts or their salt-derived counterparts [49,50]. The improvement of selectivity is attributed to the strong metal–metal interaction within heterometalic NPs and to the better dispersion on the surface. Most heterogeneous catalysts based on clusters are used in hydrogenation [50–57] and in Fischer–Tropsch reactions [58,59].

In this paper, we report the preparation of bimetallic nanoparticles supported on an ordered mesoporous carbon. The carbonaceous material was first functionalized with neutral chelating phosphine or charged ammonium groups in order to introduce anchoring points for bimetallic molecular clusters. The grafted clusters were then converted into nanoparticles by gentle thermolysis. To the best of our knowledge, this is also the first example of phosphine-functionalized OMC, which could be used as support for a wide range of catalytically active species, including homogeneous complexes.

2. Experimental

All manipulations were carried out under N_2 using standard Schlenk techniques. The solvents were distilled or degassed before use, stored under nitrogen on molecular sieves, and the obtained products were stored under Ar in a glovebox. The mesoporous carbon, noted Cm, was prepared as a replica of SBA-15 following the route described by Ryoo et al. [12,13]. Functionalized supports, Cm-PPh_2 and Cm-NMe_3^+, were prepared according to procedures described elsewhere [60]. All mentioned reactants were commercially available and used as received. Triruthenium dodecacarbonyl ($[Ru_3(CO)_{12}]$) was supplied by Alfa Aesar. Chloro(triphenylphosphine) gold ($Au(PPh_3)Cl$), bis(triphenylphosphoranylidene) ammonium chloride (PPNCl), dichloro(1,5-cyclooctadiene)platinum ($Pt(COD)Cl_2$), tetraphenylphosphonium chloride (PPh_4Cl), ethylenediamine ($H_2N(CH_2)_2NH_2$), paraformaldehyde ($(CH_2O)_n$), methyl trifluoromethanesulfonate ($CF_3SO_3CH_3$) and iron pentacarbonyl ($Fe(CO)_5$) were supplied by Aldrich. Thionyl chloride ($SOCl_2$), dicobalt octacarbonyl ($Co_2(CO)_8$) and tetraethylammonium bromide (NEt_4Br) were supplied by Acros Organics. Diphenylphosphine ($HPPh_2$) and 2-dimethylaminoethylamine ($H_2N(CH_2)_2N(CH_3)_2$) were supplied by Fluka. Nitric acid 65% was supplied by VWR and hydrochloric acid 36% by Fisher Scientific.

2.1. Functionalization of the mesoporous carbon

2.1.1. Oxidation of Cm to give Cm-ox [61]

The amount of oxygenated functional groups at the surface of the starting mesoporous Cm carbon support was increased by an acid treatment with HNO_3. In a typical experiment, 500 mg of Cm were placed in a 100 ml round-bottom flask with 20 ml HNO_3 1 mol/l or 2.5 mol/l. The mixture was stirred for 24 h at 110 °C (reflux). Then, it was filtered and extensively washed with distilled water until neutral pH. The resulting powder was dried under vacuum at 70 °C during 16 h. The Cm-ox sample oxidized with 1 mol/l nitric acid was selected for the next steps. The surface O/C ratio of this sample was determined by XPS to be equal to 0.125. Based on

previous work [61], the number of acidic functions was estimated at 1.7 mmol/g.

2.1.2. Addition of $SOCl_2$ on Cm-ox to give Cm-Cl

In a 100 ml round-bottom flask, 500 mg of Cm-ox were introduced and degassed overnight at 120 °C. Then, 30 ml of toluene were introduced together with 3 ml of $SOCl_2$. The mixture was refluxed (120 °C) for 5 h, filtered, and the obtained powder was extensively washed with toluene and dried under vacuum for several hours to give Cm-Cl.

2.1.3. Addition of $H_2N(CH_2)_2NR_2$ on Cm-Cl to give Cm-NR_2

In a 100 ml round-bottom flask, 450 mg of Cm-Cl were introduced together with 30 ml toluene. Then, 1.3 equiv. (with regard to the number of acidic functions estimated in 450 mg of oxidized Cm) of $NH_2(CH_2)_2NR_2$ (where R = H or CH_3) were added (0.99 mmol, 0.07 ml for R = H; 0.99 mmol, 0.11 ml for R = CH_3). The mixture was refluxed (120 °C) for 4 h to give Cm-NH_2 or Cm-NMe_2. Finally, the solid was filtered off, extensively washed with toluene and dried under vacuum for several hours.

2.1.4. Addition of $HPPh_2$ on Cm-NH_2 to give Cm-PPh_2

In a 100 ml round-bottom flask, 2.5 equiv. (with regard to the number of acidic functions estimated in 400 mg of oxidized Cm) of $HPPh_2$ (1.7 mmol, 0.29 ml), and CH_2O (1.7 mmol, 51 mg) were introduced with 7.5 ml of methanol. The mixture was stirred at 70 °C for 10 min and then cooled down to room temperature. At the same time, 400 mg of Cm-NH_2 were introduced with 12.5 ml of methanol in a 100 ml round-bottom flask. Once the first mixture reached room temperature, it was added to the Cm-NH_2 suspension and stirred for 15 min at room temperature. Then, 25 ml of toluene were added and the solution was stirred at 70 °C for 24 h, to give Cm-PPh_2. Finally, the solid was filtered out, extensively washed with methanol and dried under vacuum for several hours.

2.1.5. Addition of $CF_3SO_3CH_3$ on Cm-NMe_2 to give Cm-NMe_3^+

In a 100 ml round-bottom flask, 400 mg of Cm-NMe_2 were introduced together with 200 ml of acetone. Then, 3 equiv. (with regard to the number of acidic functions estimated in 400 mg of oxidized Cm) of methyl trifluoromethanesulfonate were added (2.3 mmol, 0.25 ml). The suspension was stirred at room temperature for 24 h, filtered, extensively washed with acetone and finally dried under vacuum for several hours to give Cm-NMe_3^+.

2.2. Synthesis of clusters (see Annex 1 in Supplementary data for infrared spectra)

Cluster $[HFeCo_3(CO)_{12}]$ (**1**) was obtained in 50% yield from $Fe(CO)_5$ and $Co_2(CO)_8$ [58,62]. IR ν_{CO} (CCl_4) = 2100 (w), 2059 (s), 2050 (s), 2027 (m), 1986 (m), 1883 cm^{-1} (s). Anal (calc.) = C 22.43 (25.30), H 0.23 (0.18) %. Cluster $(NEt_4)[FeCo_3(CO)_{12}]$ (**2**) was obtained in 80% yield from $Fe(CO)_5$ and $Co_2(CO)_8$ [58,62]. IR ν_{CO} (acetone) = 2063 (w), 2005 (s), 1970 (w), 1932 (m), 1823 cm^{-1} (m). Anal (calc.) = C 34.17 (34.36), H 2.88 (2.88), N 1.99 (2.00) %. Cluster $[Ru_6C(CO)_{17}]$ (**3**) was obtained in 71% in an autoclave from $[Ru_3(Co)_{12}]$ [63]. IR ν_{CO} = 2068 (s), 2047 (s) cm^{-1}. Cluster $[Ru_5C(CO)_{15}]$ (**4**) was obtained in 89% yield from cluster **3** in an autoclave [63]. IR ν_{CO} (hexane) = 2068 (s), 2034 (m), 2018 (w) cm^{-1}. $(PPN)_2[Ru_6C(CO)_{16}]$ and $(PPN)_2[Ru_5C(CO)_{14}]$ were obtained by reduction in KOH/MeOH [64] with a yield of 97 and 96%, respectively. Cluster $[Ru_6PtC(CO)_{16}(COD)]$ (**5**) was obtained in 31% yield by addition of $Pt(COD)Cl_2$ to $(PPN)_2[Ru_6C(CO)_{16}]$ [64]. IR ν_{CO} = 2078 (m), 2035 (s), 2002 (m), 1975 (w), 1943 (w) 1821 (w) cm^{-1}. Anal (calc.) = C 20.59 (21.92), H 1.50 (0.88) %. Cluster $[Ru_5PtC(CO)_{14}(COD)]$ (**6**) was obtained in 67% yield by the reaction between $Pt(COD)Cl_2$ and $(PPN)_2[Ru_5C(CO)_{14}]$ [64]. IR ν_{CO} = 2077 (m), 2050 (s), 2033 (s), 2011 (s), 1989 (w), 1966 (w) 1818 (w) cm^{-1}. Anal (calc.) = C 22.43 (22.78), H 1.10 (1) %. Cluster $[Ru_6C(CO)_{16}(Au\{PPh_3\})_2]$ (**7**) was prepared by reacting 100 mg of $(PPN)_2[Ru_6C(CO)_{16}]$ (0.0466 mmol) with 2 equiv. of $Au(PPh_3)Cl$ (46.1 mg, 0.0933 mmol) in 10 ml dichloromethane. The mixture was stirred at room temperature for 1 h, then filtered and the solvent was removed under reduced pressure. The obtained powder was purified by column chromatography on silica (hexane/dichloromethane 50/50) to give **5** as a dark red powder (77.7 mg, 84%). IR ν_{CO} = 2067 (w), 2049 (s), 2017 (vs), 1965 (w), 1821 (m) cm^{-1} [65]. Anal (calc.) = C 32.15 (32.07), H 1.64 (1.52) %. Cluster $[Ru_5C(CO)_{14}(Au\{PPh_3\})_2]$ (**8**) was obtained in 75% yield by addition of $Au(PPh_3)Cl$ to $(PPN)_2[Ru_5C(CO)_{14}]$ [66]. IR ν_{CO} = 2065 (m), 2035 (m), 2020 (s), 2008 (s), 1975 (m), 1845 (w) cm^{-1}. Anal (calc.) = C 33.31 (33.51), H 1.64 (1.65) %. Cluster $[Ru_4C(CO)_{12}(Au\{PPh_3\})_2]$ (**9**) was obtained in 67% yield from cluster **8** in an autoclave [67]. IR ν_{CO} = 2064 (vw), 2032 (s), 2022 (s), 2008 (w), 1990 (m), 1954 (w) cm^{-1}. Anal (calc.) = C 34.94 (35.22), H 1.71 (1.81) %. Cluster $[Ru_5PtC(CO)_{15}(Au\{PPh_3\})_2]$ (**10**) was obtained in 73% yield by reaction between $Au(PPh_3)Cl$ and $(PPh_4)_2[Ru_5PtC(CO)_{15}]$ [68]. IR ν_{CO} = 2068 (m), 2038 (s), 2015 (vs), 1968 (m), 1859 (m), 1834 (m) cm^{-1}. Anal (calc.) = C 30.55 (30.45), H 1.70 (1.47) %.

2.3. Grafting of clusters

The amount of cluster engaged in each grafting experiment correspond to a theoretical 5 wt.% metal loading on the support after ligands removal. In the case of cluster **1**, 12.2 mg of cluster **1** was stirred with 95 mg of support in 20 ml toluene or THF at room temperature for 5 days in the dark. The solid was filtered, washed with solvent and dried at room temperature under vacuum. For cluster **2**, 15 mg of this cluster was stirred with 95 mg of support in a 1:1 mixture of acetone and THF (total volume = 20 ml) at room temperature for 5 days in the dark. The solid was filtered washed with acetone and dried at room temperature under vacuum. For clusters **3**–**10**, the procedure was the same for all clusters. For example, 8.7 mg of cluster **3** was stirred with 95 mg of Cm-PPh_2 in a 1:1 mixture of toluene and dichloromethane (total volume = 20 ml) at room temperature for 5 days in the dark. The solid was filtered, washed with dichloromethane and dried at room temperature under vacuum.

The supported clusters were then submitted to a thermal treatment in a tubular oven STF 16/450 from CARBOLITE. The samples were placed into porcelain combustion boats and heated under N_2 stream at 200 °C for cluster **1**, 300 °C for 1 h for clusters **2**–**6** and at 350 °C for 1 h for clusters **7**–**10** (heating ramp: 100 °C/h).

2.4. Physico-chemical methods of characterization

Infrared spectra of the clusters were recorded in dichloromethane solution on a BRUKER EQUINOX 55 spectrometer with a solution cell from PERKIN ELMER.

The elemental analyses (C, H, N) of clusters were realized by the Analytical Chemistry service of University College London (UK).

The elemental analyses (C, H, N, O) of supports were realized by MEDAC Ltd., UK.

XPS analyses were performed on a Kratos Axis Ultra spectrometer (Kratos Analytical, Manchester, UK) equipped with a monochromatized aluminum X-ray source (powered at 10 mA and 15 kV). The sample powders were pressed into small stainless steel troughs mounted on a multi specimen holder. The pressure in the analysis chamber was about 10^{-6} Pa. The angle between the normal to the sample surface and the direction of photoelectrons collection was about 0°. Analyses were performed in the hybrid lens mode, the resulting analyzed area being 700 μm × 300 μm. The pass energy was set at 160 eV for the survey scan and 40 eV for narrow scans. In the latter conditions, the full width at half maximum (FWHM)

Table 1
Constraints for XPS results treatment.

Analytical peaks		Area ratio	$\Delta(B-A)$ (eV)
A	*B*	*B*/*A*	
Cl $2p_{3/2}$	Cl $2p_{1/2}$	0.500	1.6
S $2p_{3/2}$	S $2p_{1/2}$	0.500	1.18
P $2p_{3/2}$	P $2p_{1/2}$	0.500	0.84
Co $2p_{3/2}$	Co $2p_{1/2}$	0.500	14.97
Ru $3d_{5/2}$	Ru $3d_{3/2}$	0.667	4.17
Pt $4f_{7/2}$	Pt $4f_{5/2}$	0.750	3.33
Au $4f_{7/2}$	Au $4f_{5/2}$	0.750	3.67

of the Ag $3d_{5/2}$ peak of a standard silver sample was about 0.9 eV. Charge stabilization was achieved by using the Kratos Axis device. The following sequence of spectra was recorded: survey spectrum, C 1s, O 1s, N 1s, Cl 2p, S 2p, P 2p, Co 2p or Pt 4f and/or Au 4f and C 1s again to check for charge stability as a function of time and the absence of degradation of the sample during the analyses. The C-(C,H) component of the C1s peak of carbon was fixed to 284.8 eV to set the binding energy scale. Spectra were decomposed with the CasaXPS program (Casa Software Ltd., UK) with a Gaussian/Lorentzian (70/30) product function and after subtraction of a linear baseline. Molar fractions were calculated using peak areas normalized on the basis of acquisition parameters, experimental sensitivity factors and transmission factors provided by the manufacturer. The constraints used for decomposition of p, d and f doublets are summarized in Table 1 with the FWHM ratio equal to 1. Given the superposition of the C 1s and the Ru $3d_{5/2}$ peak, these constraints were particularly important in order to quantify ruthenium. The following method was used: a Gaussian/Lorentzian (85/15) was placed at the position of the Ru $3d_{5/2}$ peak, which is visible on the right-hand side (lower binding energy side) of the C 1s peak. The contribution of the Ru $3d_{5/2}$ peak to subtract from the carbon component was calculated by reference to the Ru $3d_{5/2}$ peak by placing another Lorentzian/Gaussian (85/15) at 4.17 eV toward higher binding energy, and imposing an area ratio equal to 0.667. Because of this problem of overlap, the experimental error on the Ru surface atomic concentration is high and therefore the Ru/C ratios have to be taken with caution.

The nitrogen adsorption–desorption isotherms were measured on a ASAP 2020 instrument from MICROMERITICS at 77 K. The sample was degassed for several hours at 200 °C before analysis. The specific surface area was calculated from the adsorption data using the Brunauer–Emmet–Teller (BET) method. The pore size distribution was obtained from the adsorption branch by using Barrett–Joyner–Halenda (BJH) method.

Cobalt atomic absorption measurements were carried out on a PERKIN ELMER 3110 atomic absorption spectrometer. A calibration curve was realized from a Co standard solution with a concentration of 1 g/l (Fluka).

Platinum, gold and ruthenium atomic emission measurements were carried out on a ICAP6500 spectrophotometer from Thermo Scientific (ICP-AES).

TOF-SIMS measurements were performed with an IONTOF V spectrometer. The sample was bombarded with pulsed Bi_3^+ ions (30 keV). The analyzed area used in this work was a square of 500 μm × 500 μm and the data acquisition time was 60 s. On insulating samples (such as the pure clusters), charge effects were compensated by means of an interlaced pulsed electron flood gun (E_k = 20 eV). With these parameters, the primary ion dose density was lower than 10^{11} Bi_3^+/cm^2. The powders were pressed with a spatula onto a double-sided silver adhesive sheet (SPI #5070).

TGA analyses of the clusters were recorded on a SDT 2960 simultaneous DSC–TGA instrument from TA Instruments. These analyses were carried out with a heating ramp of 10 °C/min and under N_2 flow (100 ml/min) and the samples were placed into alumina containers.

SEM images were obtained with a FEG Digital Scanning Microscope (DSM982 Gemini from LEO), equipped with a EDXS detector (Phoenix CDU LEAP). The samples were fixed by using double-sided conducting adhesive tape onto 5 mm diameter aluminum specimen stubs from Agar Scientific.

TEM images were obtained with a LEO 922 OMEGA energy filter Transmission Electron Microscope. The samples were suspended in hexane under ultrasonic treatment, then a drop of the supernatant was deposited on a holey carbon film supported on a copper grid, which was dried overnight under vacuum at room temperature before analysis.

3. Results and discussion

3.1. Supports

The mesoporous carbon support was functionalized in order to introduce anchoring sites to optimize the dispersion of the grafted clusters on its surface. Two different strategies [60,69] were envisaged as illustrated in Fig. 1. The first step, in both cases, consists in increasing the number of surface acidic functions by treatment with

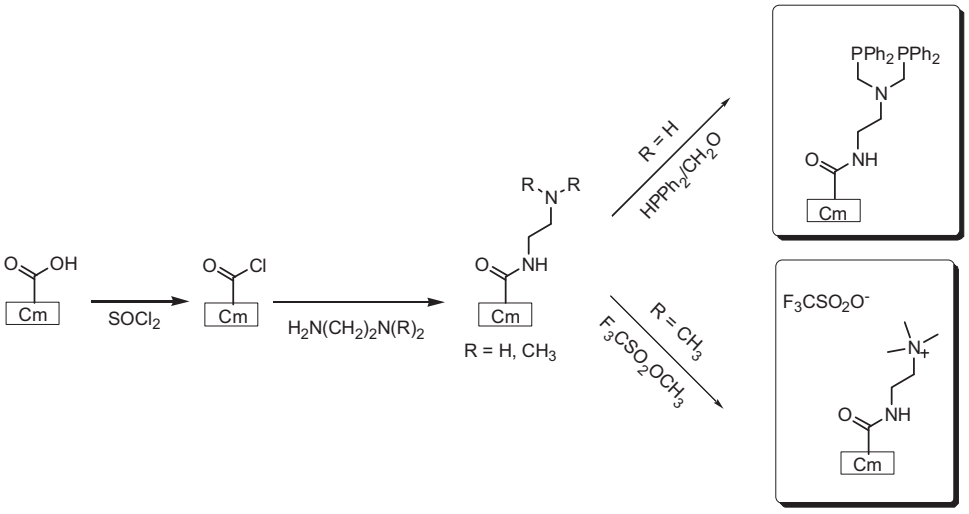

Fig. 1. Functionalization of mesoporous carbon.

Table 2
XPS results before and after oxidation by HNO_3.

	O/C	N/C
Cm	0.03	–
Cm-ox 1 mol/l	0.12	0.01
Cm-ox 2.5 mol/l	0.16	0.03

nitric acid. Then, the carboxylic acid groups can be converted into acyl chloride groups by treatment with thionyl chloride. The acyl chloride-functionalized carbon is then susceptible to react with diamines to gives amide bonds. In the last step, phosphines or ammonium groups are grafted on the terminal pendant amines.

Various characterization methods were used to estimate the degree of functionalization of the supports and to examine their textural properties at each step of functionalization. On the one hand, elemental analysis was used to determine the total oxygen content, as well as the phosphorous or nitrogen content. On the other hand, XPS allowed an estimation of the contents in surface elements and furthermore, peaks decomposition allowed to determine the nature of the introduced functions. Finally, measurements of specific surface area and porosity were realized to assess the impact of functionalization on the textural parameters of the support.

3.1.1. Oxidation of mesoporous carbon

The most commonly used oxidant for carbonaceous materials is an aqueous solution of nitric acid [8,9]. Oxidation with nitric acid is quite controllable, simply by tuning the acid concentration, temperature and treatment duration. Our procedure of oxidation is based on previous work on activated carbon [61]. Here, the only parameter varied was the concentration of nitric acid. It is known that the use of nitric acid to functionalize mesoporous carbon leads predominantly to the formation of carboxyl groups [70]. The increase in the number of acid functions was followed by XPS, via quantification of O 1s and C 1s peaks (Table 2). An increase of the O/C ratio was observed with increasing nitric acid concentration. However, when functionalizing with 2.5 mol/l HNO_3, damage in the sample was observed by SEM, in accordance with literature [9] (see Supplementary data, Fig. S1). The next steps were therefore carried out with the sample oxidized with HNO_3 1 mol/l.

To determine the types of functions present on the surface of the supports, it is possible to decompose XPS peaks into several components. The C 1s peak can be fitted with a number of components, but due to the strength of the shake-up tail relative to the low concentration of various oxide groups, the procedure cannot be considered as highly reliable. However, an increase in the region of 286–289 eV was observed (Fig. 2(a)) and corresponds to oxygen atoms bound to carbon. The decomposition of the O 1s spectrum results in two main peaks (Fig. 2(b)): oxygen doubly bound to carbon (C═O) in quinones, ketones, and aldehydes at 531.5–532 eV, and oxygen singly bound to carbon (C—O) in ethers and phenols at about 533 eV. Because oxygen atoms in esters, carboxyls, anhydrides and pyrones are involved in both single and double bonds with carbon atoms, these groups contribute to both above-mentioned peaks [71]. A third peak was observed at 535–536 eV. In the literature [72], this peak is often attributed to water, O_2 or CO_2. The decomposition of the N 1s peak results in three components (Fig. 2(c)): two components at 399–400 eV corresponding to amine or amide and one component at ~406 eV corresponding to nitro groups. Indeed, it is known that nitric acid oxidation proceeds via nitronium ion NO_2^+ which is believed to be able to attack the aromatic bonds [73]. No nitrogen was observed in the case of the pristine support.

The carbonaceous samples were also characterized by elemental analysis to determine their mass composition. Analysis of the oxidized supports shows a decrease of the quantity of carbon, coupled with an increase in the oxygen percentage (Table 3). In this case, the oxygen percentage was measured by direct measure, not by difference. If we compare the O/C ratios determined by XPS and by elemental analysis, the same values were obtained for pristine support but for Cm-ox functionalized with HNO_3 1 mol/l, the value obtained by elemental analysis is 2 times higher than by XPS. Probably, most of the oxidation takes place within the mesopores and the internal surface is not accessible by XPS which is a surface analysis.

3.1.2. Functionalization to form –PPh_2 or –NMe_3^+ surface groups

3.1.2.1. X-ray photoelectron spectroscopy. After each functionalization step (Fig. 1), a black powder was obtained and characterized

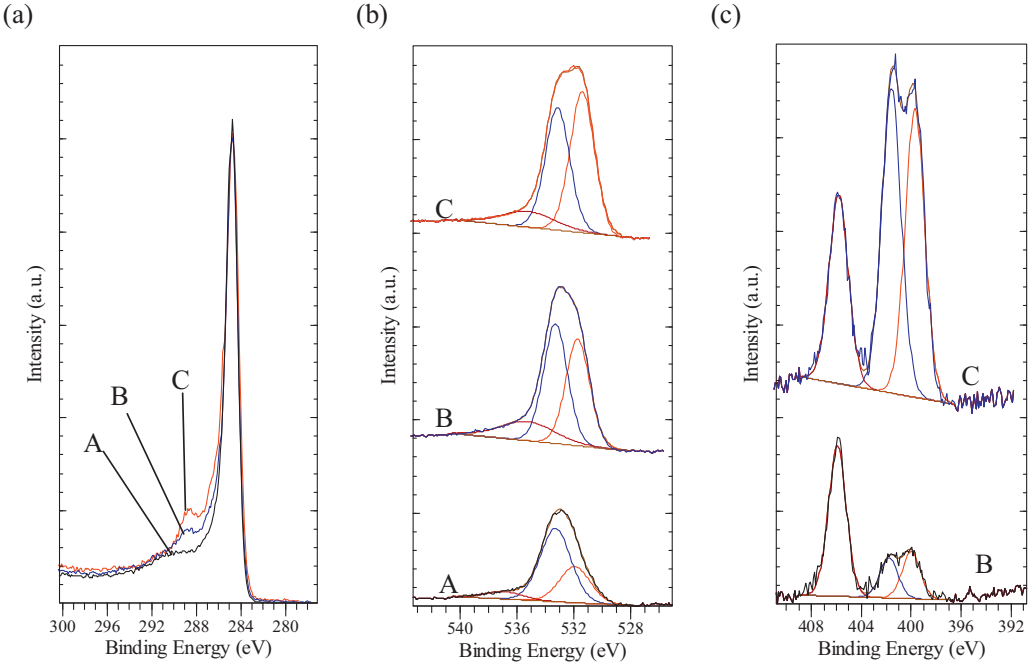

Fig. 2. XPS spectra of Cm (A), Cm-ox 1 mol/l (B) and Cm-ox 2.5 mol/l (C) in the (a) C 1s, (b) O 1s and (c) N 1s regions.

Table 3
Elemental analyses before and after oxidation by HNO_3.

Support	C (wt.%)	H (wt.%)	N (wt.%)	O (wt.%)	O/C (mass)	O/C (mol)
Cm	88.26	1.82	<0.10	4.01	0.04	0.03
Cm-ox 1 mol/l	70.22	2.33	1.12	22.07	0.31	0.23

Table 4
XPS results for the functionalization of Cm.

XPSAtomic ratio	Cm	Cm-ox	Cm-Cl	Cm-NH_2	Cm-NMe_2	Cm-PPh_2	Cm-NMe_3^+
O/C	0.033	0.088	0.087	0.061	0.072	0.058	0.123
Cl/C	–	–	0.007	0.005	0.002	0.002	0.002
N/C	–	0.010	0.017	0.055	0.054	0.041	0.043
P/C	–	–	–	–	–	0.005	–
S/C	–	–	0.003	0.002	0.002	–	0.020
F/C	–	–	–	–	–	–	0.061
F/N	–	–	–	–	–	–	1.402
S/N	–	–	–	–	–	–	0.457

Table 5
Elemental analysis of –PPh_2 and –NMe_3^+ functionalized supports.

Support	C (wt.%)	H (wt.%)	N (wt.%)	S (wt.%)	Cl (wt.%)	P (wt.%)	F (wt.%)	P or N/C (mass)	P or N/C (mol)
Cm-PPh_2	79.00	2.43	4.92	0.54	0.79	1.19	–	0.015	0.006
Cm-NMe_3^+	69.84	2.38	3.11	3.30	0.75	–	4.18	0.044	0.038

by XPS. The results are shown in Table 4. The reaction yield of individual steps was never 100%. Nevertheless, at each step, an increase in the surface concentration of the heteroatom of interest was observed. In the ammonium functionalization route, the F/N and S/N ratios were also determined to check if the counter-ion ($CF_3SO_3^-$) is present in proportional quantity with respect to the ammonium groups. In theory, the F/N ratio must be equal to 1.5 and the S/N ratio to 0.5. It is indeed the case here.

The nature of different species present on the surface can also be determined by XPS. In the first step of functionalization ($SOCl_2$ addition), Cl and S species appear. The decomposition of the Cl 2p peaks reveals two inequivalent chlorine sites. According to literature [74,75], the more intense Cl 2p component at 200.6 eV is typical of chlorine participating in organic C—Cl bonds. The less intense component with a lower binding energy of 198.8 eV can be assigned to chloride ions which are ionically bonded to the surface. The decomposition of S 2p peak results in two components. The peak at 164 eV corresponds to sulfide and the second peak at 168.5 eV can be attributed to the sulfur from $SOCl_2$ molecules or other S containing species, including SO_2 [74]. In the second step (diamine addition), the Cl 2p peak at 200.6 eV decreased or disappeared and the N 1s peak at 400 eV increased. This last peak can be attributed to amine or amide group. Sometimes, a small peak at 402 eV (already present on the oxidized support) was also observed and can be attributed to ammonium group. The last step was different for the two types of functionalization. In the case of–NMe_3^+ functionalized mesoporous carbon, the N 1s peak at 402 eV increased and the peak at 400 eV decreased at the same time. The apparition of fluorine was also observed due to the presence of the counter-ion $CF_3SO_3^-$. In the case of phosphine functionalized support, a P peak appeared. The decomposition of P 2p peak results in two components: one at 131 eV which corresponds to diphenylphosphine and the second at 133 eV which corresponds probably to oxidized phosphine [76]. This oxidation is assumed to occur during the sample preparation for the XPS analysis, and not during the synthesis, because all steps were realized under inert atmosphere.

3.1.2.2. Elemental analysis. The carbonaceous samples were characterized by elemental analysis to determine their mass composition (Table 5). If we compare the P/C ratios determined by XPS and by elemental analysis for the –PPh_2 functionalized support, the ratios were equal. In the case of –NMe_3^+ functionalized support, the same result was observed. This means that the hetero-atom functionalization was homogeneous and occurred equally on the external surface as well as in the mesopores.

3.1.3. Nitrogen adsorption isotherms

Nitrogen adsorption isotherms were recorded for representative samples at each step of the functionalization (Fig. 3(a)). The starting support presents a typical type IV isotherm with a well-defined hysteresis loop, indicating its well-ordered mesostructure, with a very narrow pore size distribution centered at 4 nm (Fig. 4 and Table 6). Upon progressive modification of the support, the specific surface area, calculated by the BET equation, was found to decrease starting from the pristine carbon to the phosphine or ammonium-functionalized ones. This reduction is accompanied by a decrease in the total pore volume. It seems from the isotherms that in particular, the micropore volume is reduced, suggesting a progressive blocking of the micropores upon support modification, leading in fine, to a totally mesoporous material (Fig. 3(b)).

Knowing the specific surface area of the Cm-PPh_2 (S_{BET} = 424 m^2/g) and the P wt.% determined by elemental analysis (1.19 wt.%), the number of phosphine ligands present on the surface per unit of area can be calculated: ~0.6 functions per nm^2. This value must be divided by 2 because the ligand is a bidentate phosphine (2 P), so 0.3 anchoring sites per nm^2 were present on the final support. In the case of ammonium-functionalized support, the same calculations did not seem reliable because nitrogen was already present on the support before the last step of functionalization.

Table 6
Textural properties of the different supports.

	S_{BET} (m^2/g)	V_{pore} (cm^3/g)	D_{pore} (nm)
Cm	1089	0.95	3.9
Cm-ox	894	0.72	3.9
Cm-PPh_2	424	0.42	4.0
Cm-NMe_3^+	402	0.40	4.0

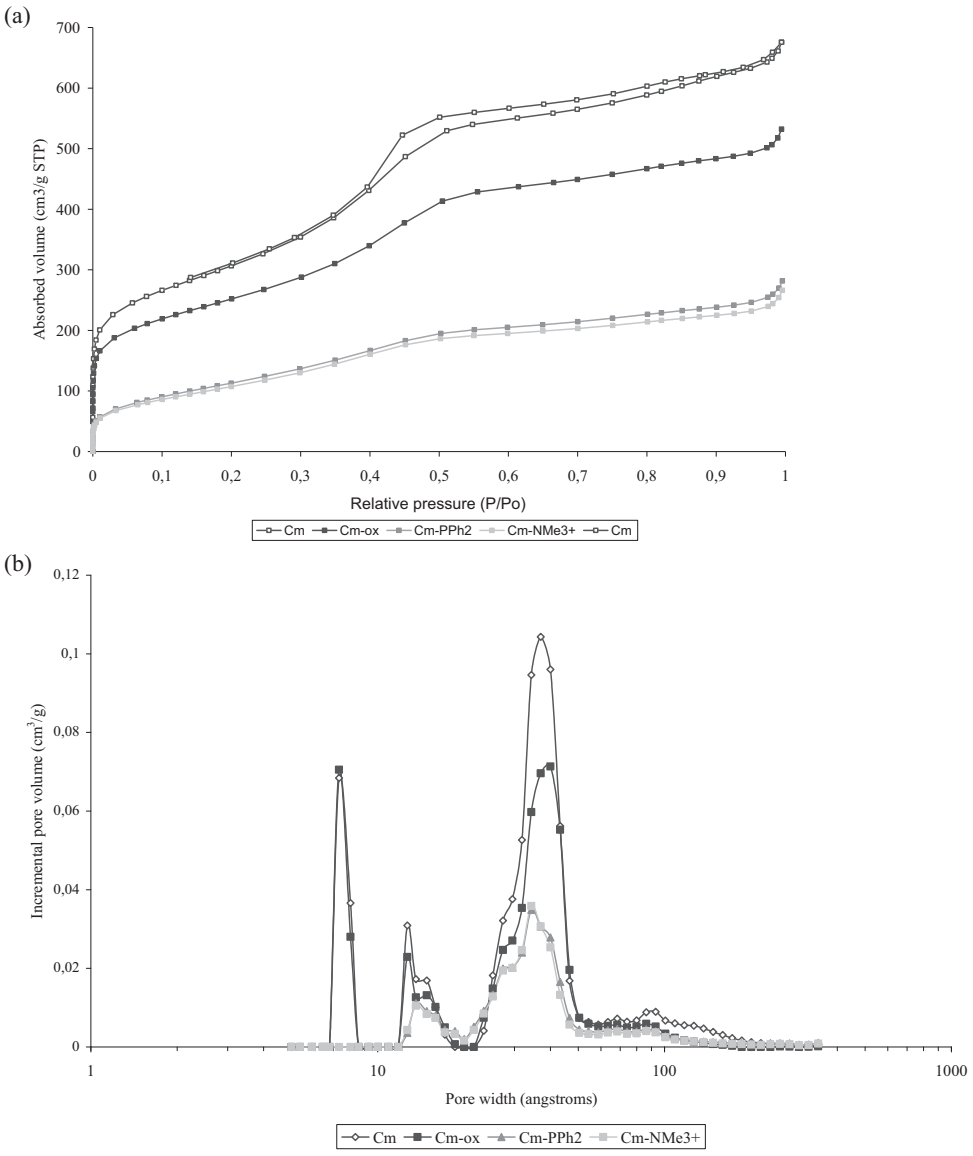

Fig. 3. (a) Nitrogen adsorption isotherms and (b) pore size distribution for functionalized Cm.

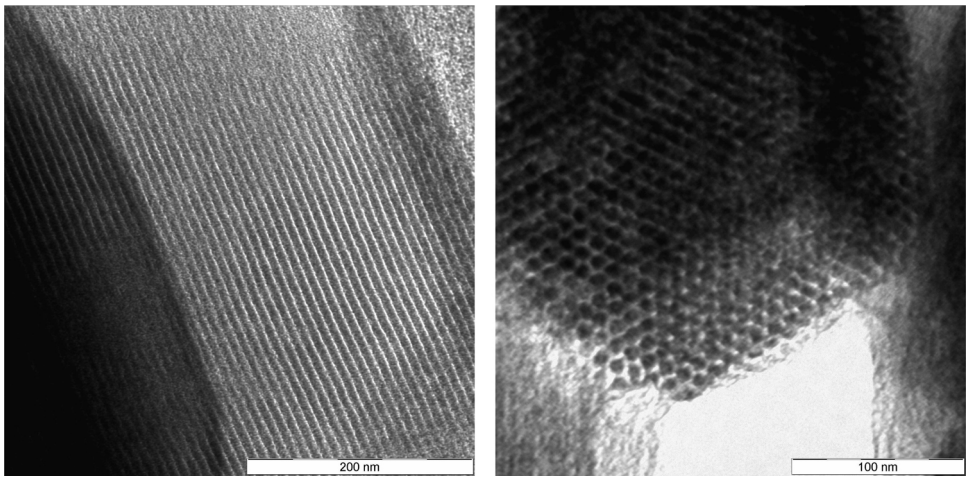

Fig. 4. TEM images of pristine mesoporous carbon.

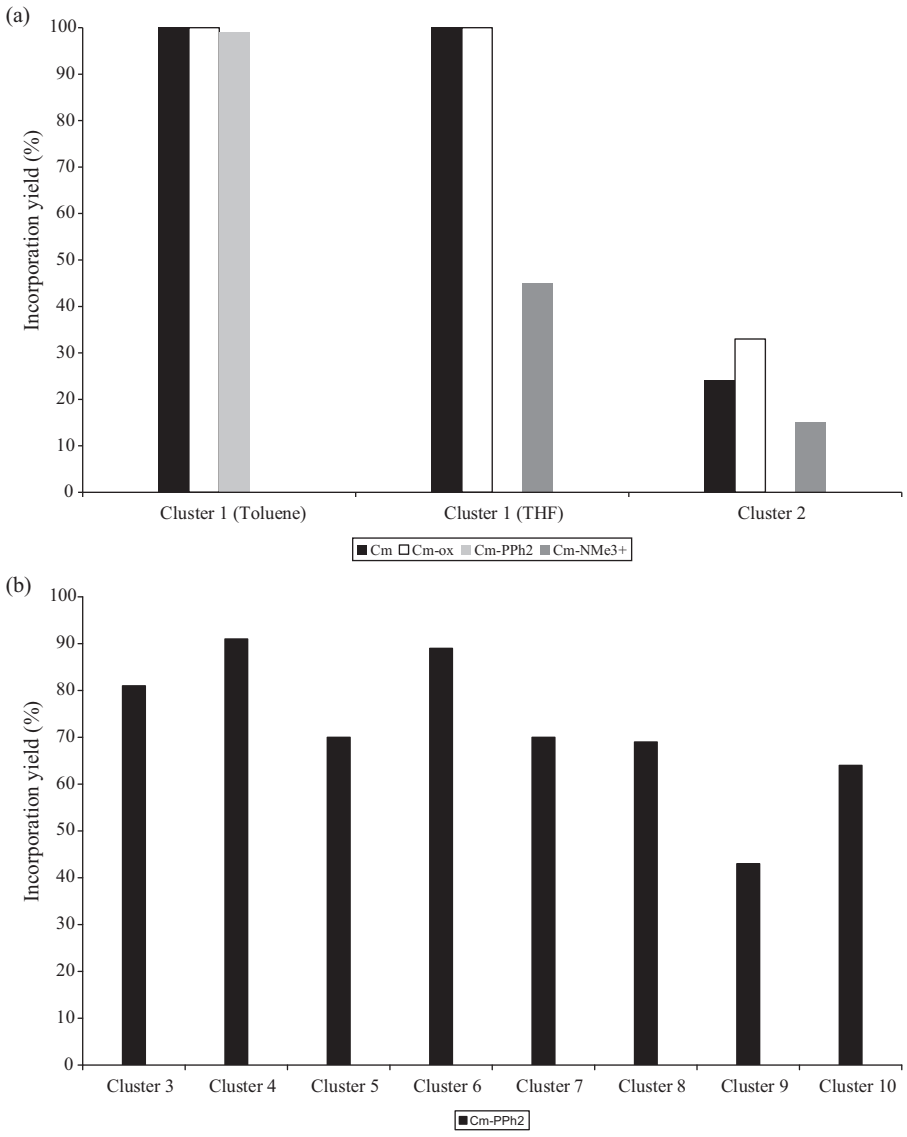

Fig. 5. Incorporation yield (%) of (a) clusters **1**–**2** and (b) clusters **3**–**10** on different mesoporous carbons.

3.2. Clusters incorporation

Clusters **1**–**10** were prepared as described previously and are listed in Table 7 (see Section 2). All clusters were unambiguously identified by their IR fingerprints in the ν_{CO} region. The ten clusters were incorporated on the functionalized mesoporous supports by stirring in a mixture of solvents, in order to optimize both cluster solubility and surface contact. The total metal loading was determined, for cluster **1** and **2**, by Co atomic absorption analysis of the synthesis filtrates (Fig. 5(a)). For cluster **3**–**10**, the total metal loading was determined by Ru, Pt and/or Au ICP analysis of the solids (Fig. 5(b)).

Table 7
Thermogravimetric analyses (under N_2).

Cluster	Weight loss (%)	Final decomposition temperature (°C)	Calculated weight loss (%)	Weight loss at selected activation temperature (%)[a]
$[HFeCo_3(CO)_{12}]$ (**1**)	56	200	59 (= 12 CO + H)	56
$(NEt_4)[FeCo_3(CO)_{12}]$ (**2**)	61	300	67 (= 12 CO + NEt_4)	61
$[Ru_6C(CO)_{17}]$ (**3**)	44	300	44 (= 17 CO)	44
$[Ru_5C(CO)_{15}]$ (**4**)	47	300	45 (= 15 CO)	47
$[Ru_6PtC(CO)_{16}(COD)]$ (**5**)	38	300	41 (= 16 CO + COD)	38
$[Ru_5PtC(CO)_{14}(COD)]$ (**6**)	38	300	41 (= 14 CO + COD)	38
$[Ru_6C(CO)_{16}(Au\{PPh_3\})_2]$ (**7**)	48	750	49 (= 16 CO + 2 PPh_3)	32
$[Ru_5C(CO)_{14}(Au\{PPh_3\})_2]$ (**8**)	49	900	50 (= 14 CO + 2 PPh_3)	26
$[Ru_4C(CO)_{12}(Au\{PPh_3\})_2]$ (**9**)	53	900	52 (= 12 CO + 2 PPh_3)	34
$[Ru_5PtC(CO)_{15}(Au\{PPh_3\})_2]$ (**10**)	45	800	46 (= 15 CO + 2 PPh_3)	30

[a] 200 °C for cluster **1**, 300 °C for clusters **2**–**6**, and 350 °C for clusters **7**–**10**.

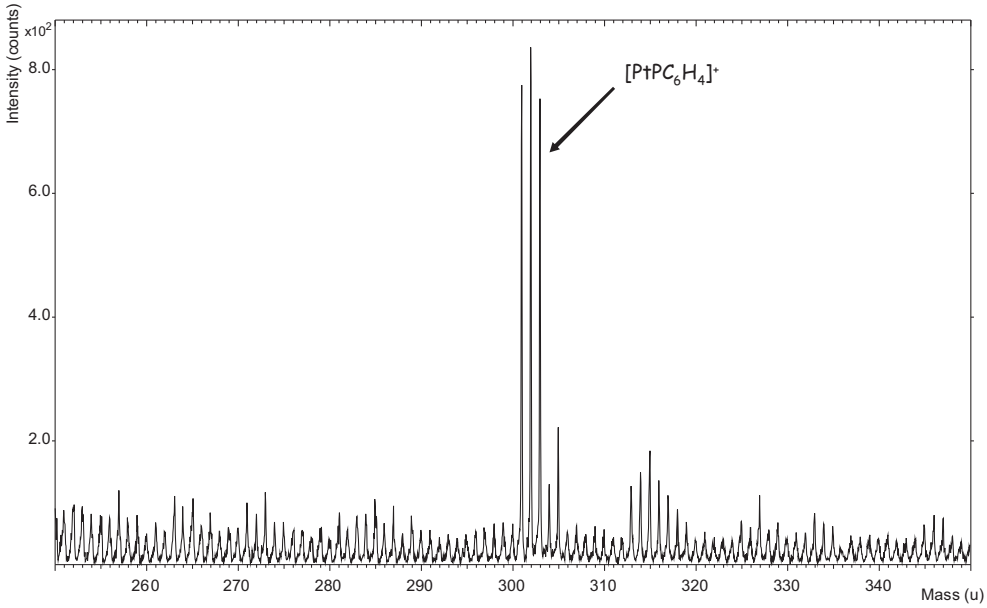

Fig. 6. Positive SIMS spectrum before thermal treatment of cluster **6** incorporated on Cm-PPh_2.

Table 8
Loading and XPS results for the incorporation of cluster **1** to **2** on Cm.

Cluster	Support	Solvent[a]	Metal loading (wt.%)[b]	XPS		
				Co/C_{calc}[c]	Co/C_{exp} before act.	Co/C_{exp} after act.
1	Cm	Tol	5.4	0.008	0.013	0.014
		THF	5.6	0.009	0.038	0.037
	Cm-ox	Tol	5.5	0.009	0.014	0.014
		THF	5.1	0.008	0.014	0.016
	Cm-PPh_2	Tol	5.1	0.008	0.017	0.017
	Cm-NMe_3^+	THF	2.2	0.003	0.004	0.005
2	Cm	THF/Acet	1.4	0.002	0.005	0.005
	Cm-ox	THF/Acet	1.6	0.003	0.005	0.005
	Cm- NMe_3^+	THF/Acet	0.8	0.001	0.002	0.002

[a] THF = tetrahydrofurane, Tol = toluene and Acet = acetone.
[b] Metal loading was calculated from incorporation yield determined by atomic absorption of cobalt in the synthesis filtrates.
[c] Calculated values are bulk molar ratios based on experimental metal loadings. The amount of Co taken into consideration for the calculations corresponds to the amount grafted on the support. The amount of C taken into consideration corresponds to the amount of support used by considering that it is only constituted of carbon.

Table 9
Loading and XPS results for the incorporation of cluster **3**–**10** on Cm-PPh_2.

Cluster	Support	Metal loading (wt.%)[a]	XPS			
			M	M/C_{calc}[b] (×100)	M/C_{exp} before act. (×100)	M/C_{exp} after act. (×100)
3	Cm-PPh_2	4.9	Ru	0.61	0.62	0.54
4	Cm-PPh_2	4.5	Ru	0.55	0.68	0.53
5	Cm-PPh_2	3.8	Ru	0.30	0.39	0.38
			Pt	0.09	0.14	0.12
6	Cm-PPh_2	4.3	Ru	0.35	0.42	0.40
			Pt	0.10	0.15	0.18
7	Cm-PPh_2	3.6	Ru	0.21	0.22	0.15
			Au	0.12	0.17	0.16
8	Cm-PPh_2	3.6	Ru	0.20	0.22	0.16
			Au	0.12	0.18	0.04
9	Cm-PPh_2	2.4	Ru	0.14	0.12	0.07
			Au	0.08	0.07	0.03
10	Cm-PPh_2	3.2	Ru	0.16	0.11	0.07
			Pt	0.04	0.07	0.05
			Au	0.09	0.12	0.08

[a] Metal loading calculated from incorporation yield determined by ICP analysis of metals in solid samples.
[b] Calculated values are bulk molar ratios based on experimental metal loadings. The amount of metal taken into consideration for the calculations corresponds to the amount grafted on the support. The amount of C taken into consideration corresponds to the amount of support used by considering that it is only constituted of carbon.

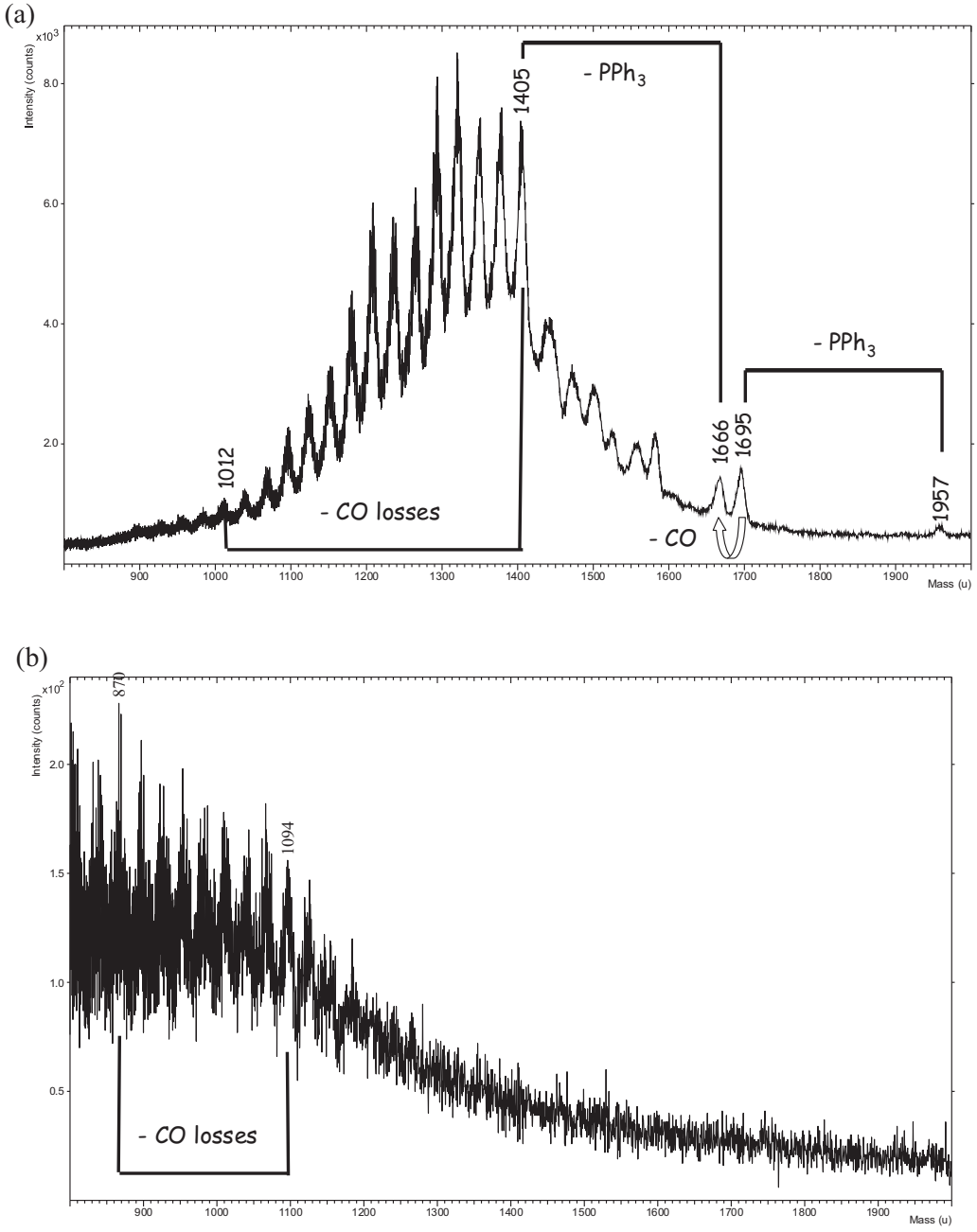

Fig. 7. Negative SIMS spectra of cluster $[Ru_6C(CO)_{15}(Au\{PPh_3\})_2]$ (**7**) before thermal treatment: (a) pure unsupported cluster as reference and (b) cluster **7** incorporated on Cm-PPh_2.

In the case of FeCo clusters, the choice of solvent is justified by the fact that cluster $[HFeCo_3(CO)_{12}]$ **1** is protonated (hence neutral) in toluene and deprotonated (hence negatively charged) in THF [60]. For cluster **1** in toluene, the incorporation yield reached 100% on the Cm-PPh_2 support. The fixation of this neutral cluster onto a support functionalized by chelating phosphine ligands occurs by ligand exchange for CO ligands present initially on the cluster. Quantitative incorporation yield was also obtained on pristine Cm and oxidized Cm-ox, used as 'blank' experiments. However, we know from previous studies [60,69], that the repartition of clusters on the support surface is less ideal when incorporated by non-specific interactions. In addition, they are then not fixed covalently on the support and are highly mobile during the thermal activation step, leading to agglomeration. Functionalization is necessary, starting from carbonyl clusters, to ensure that nanometric particles are obtained in the end. In the case of the same cluster $[HFeCo_3(CO)_{12}]$ **1** in THF, where it is deprotonated (hence negatively charged), the incorporation yield was also equal to 100% on pristine and oxidized supports but for Cm-NMe_3^+, it was only 45%. This means that the formation of ion-pairs with clusters on the surface is less efficient than the ligand exchange mechanism with the chelating phosphine. In the case of cluster **2**, which is always negatively charged, the incorporation yield was smaller in every case. These poor results can be explained by the presence of tetraethylammonium as counter-ion that stabilizes the cluster in solution and is competing with the support.

In the case of RuM (where M = Pt or Au) clusters, only Cm-PPh_2 was used for incorporation, as they are all neutral and stay so. These clusters are all able to react with a chelating phosphine group by ligand exchange, which gives the cluster core covalently attached

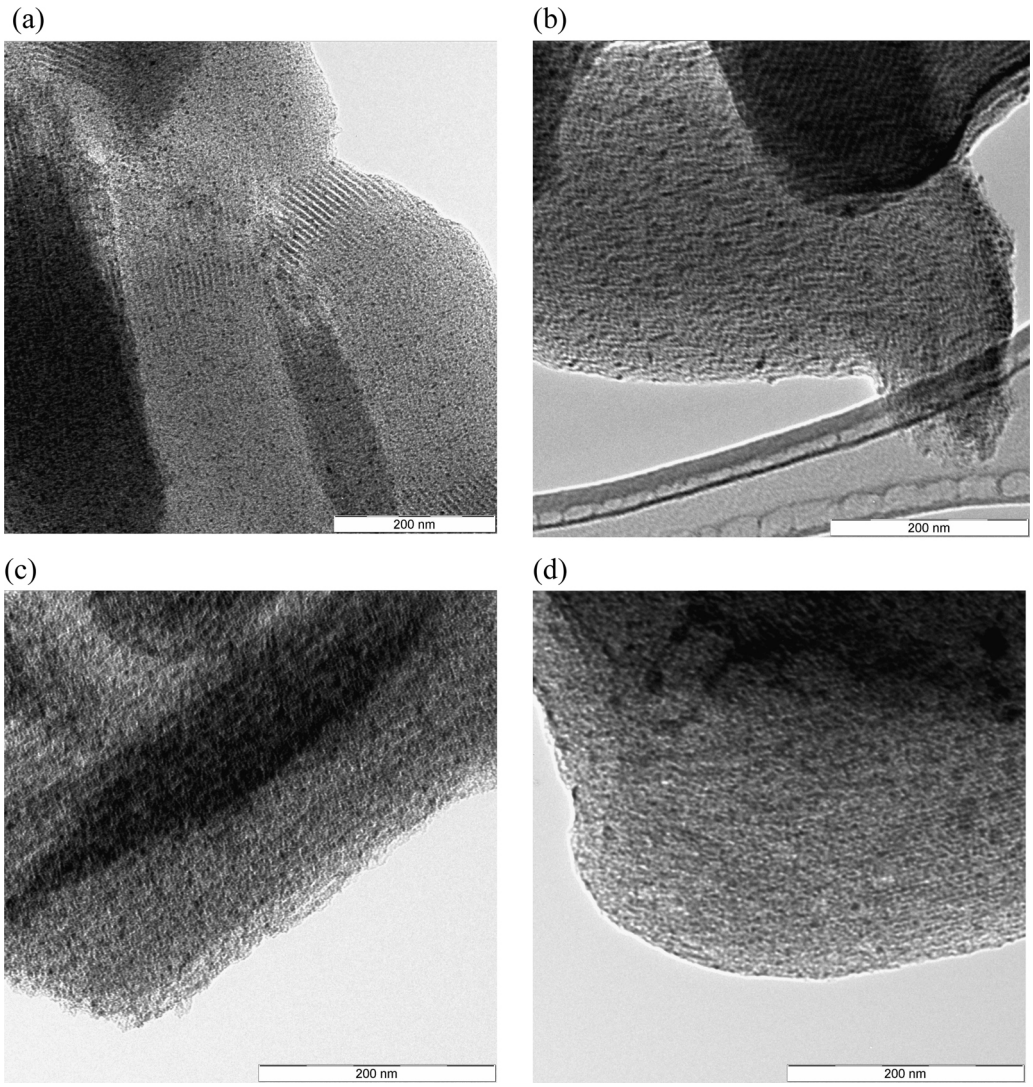

Fig. 8. TEM images of cluster $[HFeCo_3(CO)_{12}]$ (**1**) after thermal treatment: (a) on Cm (THF), (b) on Cm-ox (THF), (c) on Cm-PPh_2 and of cluster $(NEt_4)[FeCo_3(CO)_{12}]$ (**2**) after thermal treatment: (d) on Cm-ox.

to the functionalized surface. Some preliminary 'blank' tests with cluster **6** showed that no incorporation occurred on pristine Cm whereas a 100% incorporation yield could be obtained on the oxidized support. Again, we know that the oxygen-containing groups are not able to function as ligands for neutral organometallic clusters, hence lead to non-specific interactions that need to be avoided. Considering clusters **3**–**10** with the functionalized support Cm-PPh_2, the incorporation yield was, most of the time, higher than 60%, and reached 90% in the best cases (Fig. 5(b)).

Clusters **1** and **2** incorporated on the different mesoporous carbons were characterized by SIMS after cluster incorporation. The molecular peak and the typical fragmentation pattern of such clusters were not obtained. This might be ascribed to the low quantity of metal present on the support surface and/or to the location of metal species within the pores. Cluster **6** incorporated on Cm-PPh_2 and Cm-ox was also characterized by SIMS. Again, the molecular peak and the typical fragmentation pattern of such clusters were not obtained. However, the presence of metals and some specific fragments could be observed. On the SIMS spectra of $[Ru_5PtC(CO)_{14}(COD)]$ (**6**) on Cm-PPh_2 in positive mode (Fig. 6), an isotopic peak centered at m/z 302 was observed which corresponds to $[PtPC_6H_4]^+$ (centered at 302.1). The PC_6H_4 fragment originates from the phosphine groups present on the support, unequivocally proving that a reaction occurred between the cluster and the functionalized support. Indeed, it is known that the COD ligand in cluster **4** is easily exchanged for phosphines in this cluster [77].

Cluster **7** on phosphine-functionalized mesoporous carbon was also analyzed by SIMS. The SIMS spectrum obtained for the pure, unsupported cluster is displayed in Fig. 7(a). The peak with highest m/z value is observed at m/z 1957 ($[Ru_6C(CO)_{15}(Au\{PPh_3\})_2]^-$), and is followed by the successive losses of one PPh_3 ligand at m/z 1695, then 1 CO ligand and the other PPh_3 ligand at m/z 1405 ($[Ru_6Au_2C(CO)_{14}]^-$). Next, a series of peaks corresponding to CO losses up to m/z 1012 ($[Ru_6Au_2C]^-$) were observed. When cluster **7** was anchored onto Cm-PPh_2, some small peaks were observed by SIMS (Fig. 7(b)) but with a shift of m/z 197, which corresponds to one gold atom. The highest mass peak is observed at m/z 1153 ($[Ru_6Au_2C(CO)_{12}]^-$) followed by fragments corresponding to CO losses up to m/z 840 ($[Ru_6Au_2C(CO)]^-$). The same result was obtained in a previous work on activated carbon and was interpreted with the aid of model studies in solution as cluster fragmentation upon grafting [69].

After incorporation, a thermal activation was performed to obtain supported naked metal particles by removing the ligands.

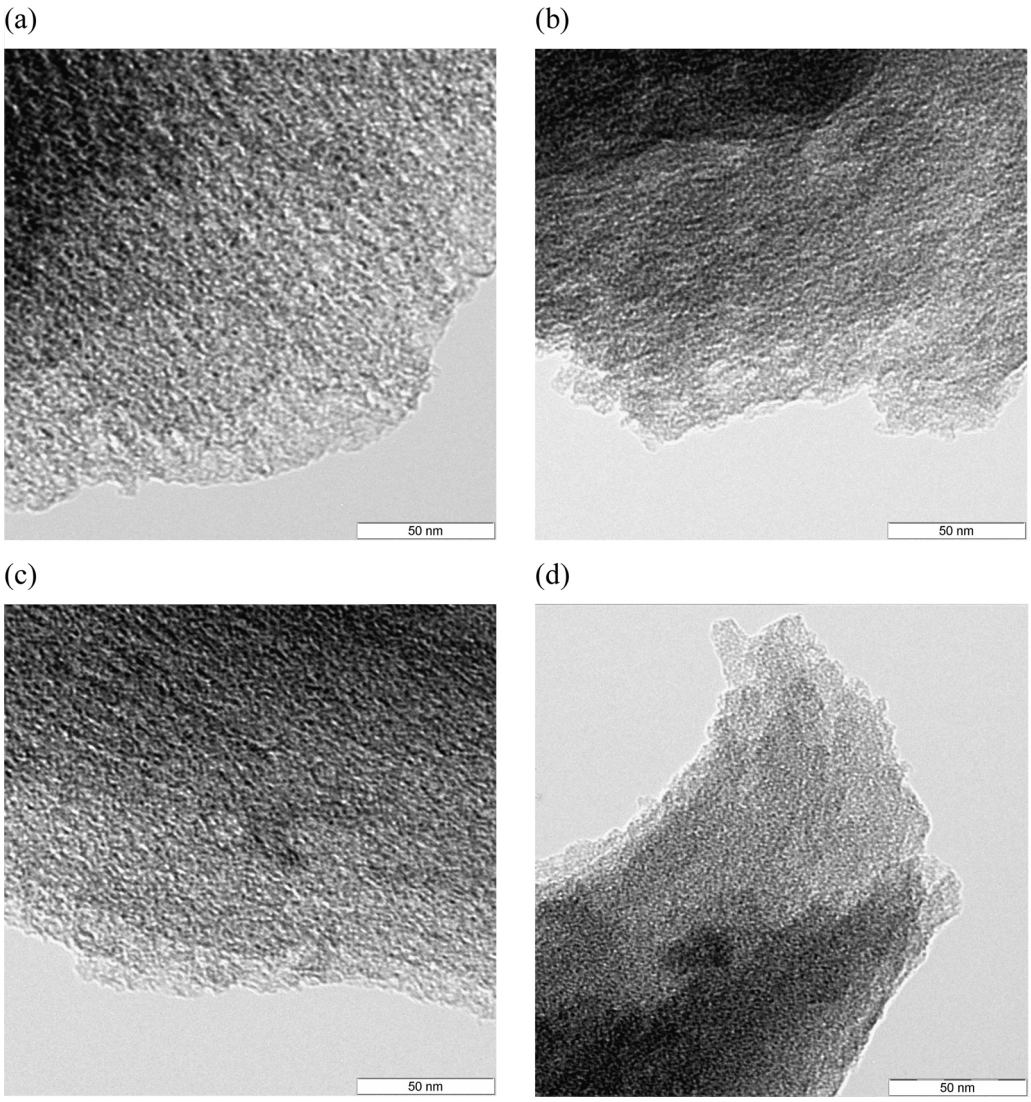

Fig. 9. TEM images of clusters **3**–**6** on Cm-PPh_2 after thermal treatment: (a) $[Ru_6C(Co)_{17}]$ (**3**), (b) $[Ru_5C(CO)_{15}]$ (**4**), (c) $[Ru_6PtC(CO)_{16}(COD)]$ (**5**) and (d) $[Ru_5PtC(CO)_{14}(COD)]$ (**6**).

Control over this step is obtained by the covalent anchoring that reduces clusters mobility and agglomeration. Moreover, thermogravimetric analyses of the pure clusters were realized to determine the optimal activation temperature (Table 7). For clusters **1**–**6** the selected temperature was the final decomposition temperature. For clusters **7**–**10**, the chosen temperature was 350 °C during 1 h under nitrogen. This temperature corresponds to the loss of the majority of ligands. Indeed, for these clusters, the ligands loss occurred in a more gradual way up to higher temperatures (800–900 °C) and the selected activation temperature is a compromise to avoid agglomeration.

The surfaces of the different samples were characterized by XPS before and after activation to determine the surface M/C ratios, and by ICP to determine bulk loadings. The metal loading determined by ICP (Tables 8–9) after activation was comprised between 1 and 6 wt.%, which depends on the number of surface functionalization sites available for clusters incorporation. It could have been majored by increasing the number of these surface sites or by repeated cluster impregnations. The XPS results are also presented in Tables 8 and 9. It should be noted that the Fe/C ratios could not be determined because the cobalt Auger line $L_3M_{45}M_{45}$ and the Fe 2p XPS peak overlap each other, while the other Fe XPS peaks are not sensitive enough to be used. The experimental M/C values before thermal treatment were equal or slightly higher than the predicted values, which are calculated based on the incorporated quantities, except for clusters **9** and **10**. The anchored clusters are therefore located on the external surface as well as within the mesopores. For clusters **1** and **2**, there is no or small differences between before and after activation, which means that there was no agglomeration during activation. By opposition, in the case of clusters **3**–**10**, the experimental values decreased after activation, which means that there was some agglomeration. This phenomenon was more important for clusters containing gold (clusters **7**–**10**). The Ru/M (M = Pt, Au) ratios were also determined by ICP and XPS (see Supplementary data, Table S1). In the case of ICP, the experimental ratios were close to the theoretical values. There was a systematic error probably due to the known difficulty of ruthenium dissolution. In the case of XPS, the experimental values were not close to the theoretical values. These differences can be explained, on the one hand, by the experimental error on the Ru surface atomic concentration determination due to overlap between the Ru $3d_{5/2}$ and C 1s peaks, and on the other hand, by fragmentation of the cluster in the case of gold-containing clusters.

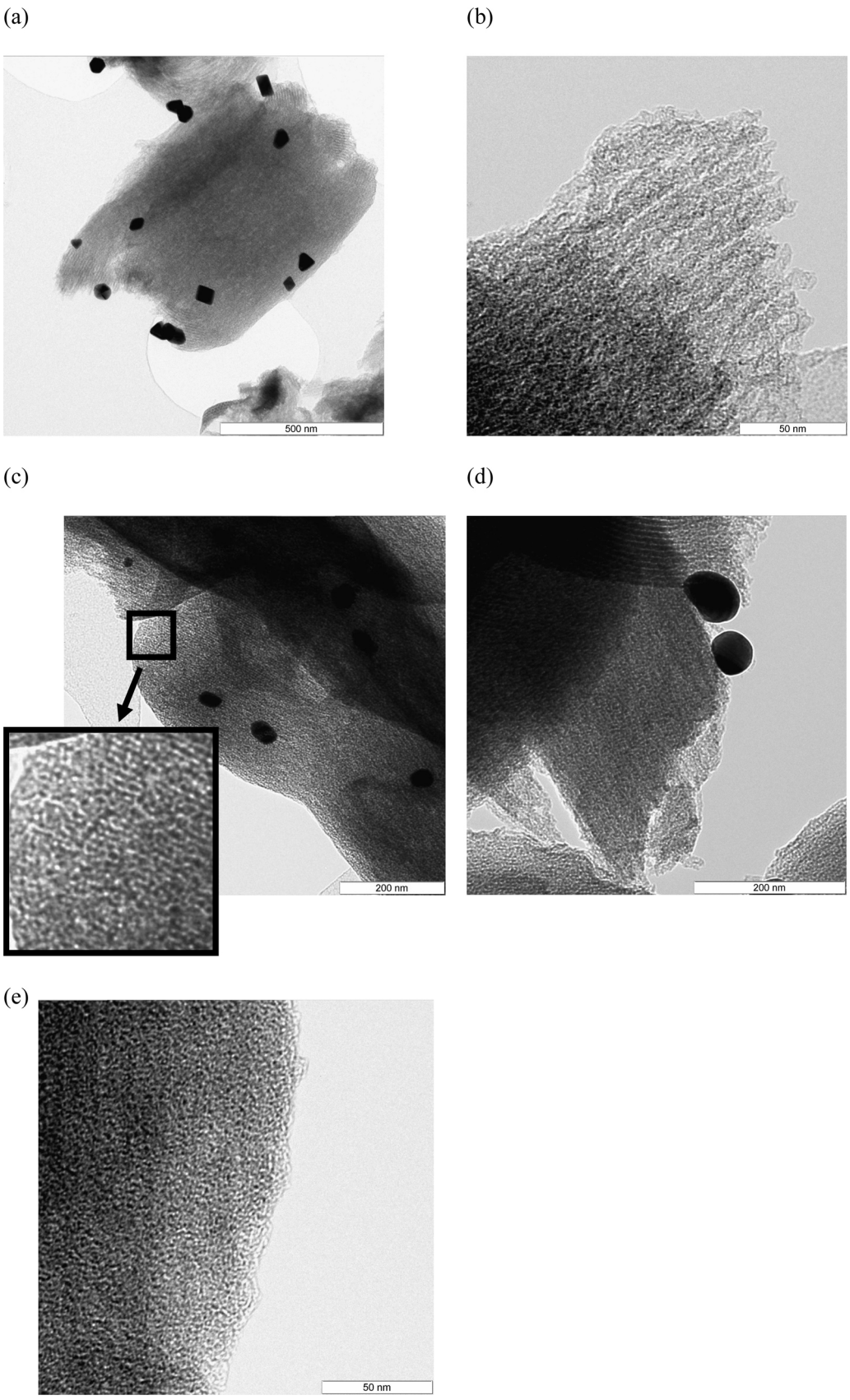

Fig. 10. TEM images of clusters **7**–**10** on Cm-PPh_2 after thermal treatment: (a) and (b) $[Ru_6Au_2C(CO)_{16}(PPh_3)_2]$ (**7**), (c) $[Ru_5Au_2C(CO)_{14}(PPh_3)_2]$ (**8**), (d) $[Ru_4Au_2C(CO)_{12}(PPh_3)_2]$ (**9**) and (e) $[Ru_5PtAu_2C(CO)_{15}(PPh_3)_2]$ (**10**).

Finally, all samples were characterized by TEM to determine the particle sizes after activation. In the case of cluster **1** (Fig. 8(a)–(c)), the size distribution was approximately the same for the three supports: between 1 and 7 nm. The particles were homogeneously distributed over the whole surface. No major difference was found between the different supports. One sample was analyzed by EDXS (see Supplementary data, Fig. S2) and both metals were observed. In the case of cluster **2** (Fig. 8(d)), particles with a size lower than 3 nm were seen with sometimes the presence of particles of 6–8 nm. For clusters containing ruthenium, two distinct cases were observed. For clusters **3**–**6**, which include Ru and RuPt clusters, the particles size was lower than 3 nm and predominantly between 1 and 2 nm (Fig. 9). The particles were homogeneously distributed on the support. However, in spite of the fact that the final particles were small, some agglomeration did occur during thermal activation because their size is slightly above the size of a single cluster (~0.4 nm). Samples with cluster **4** and **6** on Cm-PPh_2 were analyzed by EDXS (see supplementary info) and Ru was observed in both samples. For Pt, its peak overlaps with the P peak. In the case of RuAu clusters (Clusters **7–10**, Fig. 10), TEM images showed that well-dispersed nanoparticles smaller than 3 nm were also obtained, but with the concomitant presence of bigger particles of 30–70 nm. These bigger particles were analyzed by EDXS (see Supplementary data, Fig. S2), which indicates that these particles were exclusively constituted of gold. The small particles were also analyzed by EDXS (see Supplementary data), and both metals, i.e. gold and ruthenium, were observed. So for these clusters, the grafting on phosphine functionalized supports causes their fragmentation into two separate entities that are retained on the support by phosphine groups. This is in agreement with results of SIMS characterization (see above). Then, during thermal treatment, the gold atoms tend to agglomerate. It is thus more the nature of the molecular cluster precursor rather than the support that is decisive on the final nanostructured material obtained. By choosing adequately a cluster precursor known to undergo readily a ligand exchange reaction (such as that species containing the COD ligand) in conjunction with a support functionalized with a ligand moiety, we have shown that nanoparticles of heterometallic nature can be formed on a catalytically relevant support. This is not an easy matter, as proving the bimetallic nature of a particle at the nanometer size is very difficult when it has been synthesized from separated monometallic salt precursors (even by co-impregnation). Mixed-metal clusters even allow the preparation of bimetallic nanoparticles of metals that do not form alloys in the bulk. Going further in the present study, one could envision studying the effect of confinement within the mesopores by selectively functionalizing only the external or the internal surfaces and comparing the sample with nanoparticles located inside the mesopores with the one presenting the nanoparticles on the external surface in terms of catalytic activity/selectivity.

Preliminary catalytic tests were carried out in cinnamaldehyde selective hydrogenation, and the Ru_5Pt/Cm-PPh_2 catalyst (prepared from cluster (**6**)) was found to be very active, with selectivity for cinnamyl alcohol (the product of interest) higher than equivalent catalysts prepared on carbon nanotubes or carbon nanofibers using the same methodology.

4. Conclusions

A mesoporous carbon material prepared by hard-templating was functionalized and used as support for molecular precursors of hetero-metallic nanoparticles. The number of surface carboxylic acid groups was increased by nitric acid oxidation, and this was shown to occur more within the pores than on the external surface. Then, by activation with thionyl chloride followed by reaction with diamine, an amide bond was created for post-functionalization. The pendant amine groups could then be derivatized into charged ammonium or chelating phosphine groups. The functionalization was homogeneous and occurred without loss of the mesoporous structure.

The surface functions were used to immobilize bimetallic cluster compounds, via electrostatic interactions or ligand exchange. Characterization indeed showed the success of the procedure and molecular surface fragments containing both metal and ligand were highlighted by SIMS. The anchored clusters were then thermally transformed into nanoparticles denuded of organic ligands layers. Characterizations and TEM imaging demonstrated that this methodology indeed led to heterometallic nanoparticles located within the mesopores of the carbon framework. A counter-example with gold clusters that fragment upon anchoring provided a further proof of the success of the presented methodology. The obtained NP/OMC nanomaterials could find applications in a wide range of heterogeneously-catalyzed hydrogenation reactions or as superior electrodes in fuel cells.

Acknowledgements

The authors gratefully acknowledge the 'Fonds National de la Recherche Scientifique' (FNRS) and the Interuniversity Attraction Pole Programme of the Belgian State (INANOMAT P6/17), as well as the support of Fédération Wallonie-Bruxelles and the national lottery (FRFC) for financial support. They also acknowledge the 'Fonds pour la formation à la Recherche dans l'Industrie et dans l'Agriculture' (FRIA) for the research fellowship allotted to D.V. We are also grateful to J.-F. Statsijns for technical support.

Appendix A. Supplementary data

Supplementary data associated with this article can be found, in the online version, at http://dx.doi.org/10.1016/j.cattod.2014.03.017.

References

[1] J.B. Goodenough, Y. Kim, J. Power Sources 196 (2011) 6688–6694.
[2] J. Chmiola, G. Yushin, Y. Gogotsi, C. Portet, P. Simon, P.L. Taberna, Science 313 (2006) 1760–1763.
[3] E. Raymundo-Piñero, F. Leroux, F. Béguin, Adv. Mater. 18 (2006) 1877–1882.
[4] M.F.R. Pereira, S.F. Soares, J.J.M. Órfão, J.L. Figueiredo, Carbon 41 (2003) 811–821.
[5] G. Liu, J. Ma, X. Li, Q. Qin, J. Hazard. Mater. 164 (2009) 1275–1280.
[6] P. Serp, J.L. Figueiredo, Carbon Materials for Catalysis, John Wiley & Sons, Hoboken, NJ, 2009.
[7] F. Rodriguez-Reinoso, in: J.W. Patrick (Ed.), Porosity in Carbons, Wiley, UK, 1995, p. 253.
[8] A. Stein, Z. Wang, M.A. Fierke, Adv. Mater. 21 (2009) 265–293.
[9] J.L. Figueiredo, J. Mater. Chem. A 1 (2013) 9351–9364.
[10] N. Job, R. Pirard, J. Marien, J.P. Pirard, Carbon 42 (2004) 619–628.
[11] T.Y. Ma, L. Liu, Z.Y. Yuan, Chem. Soc. Rev. 42 (2013) 3977–4003.
[12] R. Ryoo, S.H. Joo, S. Jun, J. Phys. Chem. B 103 (1999) 7743–7746.
[13] S. Jun, S.H. Joo, R. Ryoo, M. Kruk, M. Jaroniec, Z. Liu, T. Ohsuna, O. Terasaki, J. Am. Chem. Soc. 122 (2000) 10712–10713.
[14] D.Y. Zhao, Q.S. Huo, J.L. Feng, B.F. Chmelka, G.D. Stucky, J. Am. Chem. Soc. 120 (1998) 6024.
[15] C.D. Liang, Z.J. Li, S. Dai, Angew. Chem. Int. Ed. 47 (2008) 3696–3717.
[16] A.H. Lu, F. Schüth, Adv. Mater. 18 (2006) 1793–1805.
[17] I. Muylaert, A. Verberckmoes, J. De Decker, P. Van Der Voort, Adv. Colloid. Interface Sci. 175 (2012) 39–51.
[18] F.Q. Zhang, Y. Meng, D. Gu, Y. Yan, Z.X. Chen, B. Tu, D.Y. Zhao, Chem. Mater. 18 (2006) 5279–5288.
[19] S. Tanaka, N. Nishiyama, Y. Egashira, K. Ueyama, Chem. Commun. (2005) 2125–2127.
[20] X.C. Zhao, A. Wang, J.W. Yan, G.Q. Sun, L.X. Sun, T. Zhang, Chem. Mater. 22 (2010) 5463–5473.
[21] D. Liu, J.H. Lei, L.P. Guo, D. Qu, Y. Li, B.L. Su, Carbon 50 (2012) 476–487.
[22] K.-I. Min, J.-S. Choi, Y.M. Chung, W.S. Ahn, R. Ryoo, P.K. Lim, Appl. Catal. A 337 (2008) 97.
[23] P. Gao, A.Q. Wang, X.D. Wang, T. Zhang, Chem. Mater. 20 (2008) 1881–1888.
[24] Y. Zhai, Y. Dou, X. Liu, S.S. Park, C.S. Ha, D.Y. Zhao, Carbon 49 (2011) 545–555.

[25] A.H. Lu, W. Schmidt, N. Matoussevitch, H. Bönnemann, B. Spliethoff, B. Tesche, E. Bill, W. Kiefer, F. Schüth, Angew. Chem. Int. Ed. 43 (2004) 4303–4306.
[26] A.H. Lu, W.C. Li, Z. Hou, F. Schüth, Chem. Commun. (2007) 1038.
[27] K.S. Ha, G. Kwak, K.W. Jun, J. Hwang, J. Lee, Chem. Commun. 49 (2013) 5141–5143.
[28] X. Wang, R. Liu, M.M. Waje, Z. Chen, Y. Yan, K.N. Bozhilov, P. Feng, Chem. Mater. 19 (2007) 2395–2397.
[29] C. Freire, A.R. Silva, in: P. Serp, J.L. Figueiredo (Eds.), Carbon Materials for Catalysis, John Wiley & Sons, Hoboken, NJ, 2009, pp. 267–307.
[30] A.R. Silva, C. Freire, B. de Castro, M.M.A. Freitas, J.L. Figueiredo, Micropor. Mesopor. Mater. 46 (2001) 211–221.
[31] K. Scholz, J. Scholz, A.J. McQuillan, G. Wagner, O. Klepel, Carbon 48 (2010) 1788.
[32] W.C. Choi, S.I. Woo, M.K. Jeon, J.M. Sohn, M.R. Kim, H.J. Jeon, Adv. Mater. 17 (2005) 446.
[33] S.H. Joo, S.J. Choi, I. Oh, J. Kwak, Z. Liu, O. Terasaki, R. Ryoo, Nature 412 (2001) 169.
[34] P.V. Samant, M.F.R. Pereira, J.L. Figueiredo, Catal. Today 102 (2005) 183.
[35] F.B. Su, J.H. Zeng, X.Y. Bao, Y.S. Yu, J.Y. Lee, X.S. Zhao, Chem. Mater. 17 (2005) 3960.
[36] F.B. Su, X.S. Zhao, Y. Wang, J.H. Zeng, Z.C. Zhou, J.Y. Lee, J. Phys. Chem. B 109 (2005) 20200.
[37] F.B. Su, H.J. Zeng, Y.J. Yu, L. Lv, J.Y. Lee, X.S. Zhao, Carbon 43 (2005) 2368.
[38] Y.L. Cao, J.M. Cao, M.B. Zheng, J.S. Liu, G.B. Ji, H.M. Ji, J. Nanosci. Nanotechnol. 7 (2007) 504.
[39] A.H. Lu, W.C. Li, Z.S. Hou, F. Schuth, Chem. Commun. (2007) 1038.
[40] Y. Wan, H.Y. Wang, Q.F. Zhao, M. Klingstedt, O. Terasaki, D.Y. Zhao, J. Am. Chem. Soc. 131 (2009) 4541.
[41] S.M. Holmes, P. Foran, E.P.L. Roberts, J.M. Newton, Chem. Commun. (2005) 1912.
[42] J. Lee, S.M. Jin, Y. Hwang, J.G. Park, H.M. Park, T. Hyeon, Carbon 43 (2005) 2536.
[43] A.H. Lu, W. Schmidt, N. Matoussevitch, H. Bonnemann, B. Spliethoff, B. Tesche, E. Bill, W. Kiefer, F. Schuth, Angew. Chem. Int. Ed. 43 (2004) 4303.
[44] T. Yu, Y.H. Deng, L. Wang, R.L. Liu, L.J. Zhang, B. Tu, D.Y. Zhao, Adv. Mater. 19 (2007) 2301.
[45] M.-L. Lin, M.-Y. Lo, C.-Y. Mou, J. Phys. Chem. C 113 (2009) 16158.
[46] G.S. Chai, S.B. Yoon, J.S. Yu, J.H. Choi, Y.E. Sung, J. Phys. Chem. B 108 (2004) 7074.
[47] L. Calvillo, M.J. Lázaro, E. García-Bordejé, R. Moliner, P.L. Cabot, I. Esparbé, E. Pastor, J.J. Quintana, J. Power Sources 169 (2007) 59.
[48] G. Álvarez, F. Alcaide, O. Miguel, L. Calvillo, M.J. Lázaro, J.J. Quintana, J.C. Calderón, E. Pastor, J. Solid State Electrochem. 14 (2010) 1027.
[49] A.C.W. Koh, L.W. Chen, W.K. Leong, T.P. Ang, B.F.G. Johnson, T. Khimyak, J.Y. Lin, Int. J. Hydrogen Energy 34 (2009) 5691.
[50] C.X. Li, W.K. Leong, Z.Y. Zhong, J. Organomet. Chem. 694 (2009) 2315.
[51] S. Chotisuwan, J. Wittayakan, B.C. Gates, J. Phys. Chem. B 110 (2006) 12459.
[52] A. Siani, B. Captain, R.D. Adams, O.S. Alexeev, M.D. Amiridis, Top. Catal. 54 (2011) 318.
[53] R. Raja, T. Khimyak, J.M. Thomas, S. Hermans, B.F.G. Johnson, Angew. Chem. Int. Ed. 40 (2001) 4638.
[54] J.M. Thomas, B.F.G. Johnson, R. Raja, G. Sankar, P.A. Midgley, Accounts Chem. Res. 36 (2003) 20.
[55] C. Vollmer, E. Redel, K. bu-Shandi, R. Thomann, H. Manyar, C. Hardacre, C. Janiak, Chem. Eur. J. 16 (2010) 3849.
[56] S.M. Yunusov, E.S. Kalyuzhnaya, H. Mahapatra, V.K. Puri, V.A. Likholobov, V.B. Shur, J. Mol. Catal. A: Chem. 139 (1999) 219.
[57] Y. Zhu, H.F. Qian, M.Z. Zhu, R.C. Jin, Adv. Mater. 22 (2010) 1915.
[58] R.S. Armstrong, T. Bell, A.F. Masters, M.A. Williams, A.L. Chaffee, Polyhedron 9 (1990) 2815.
[59] P. Moggi, G. Predieri, F. Di Silvestri, A. Ferretti, Appl. Catal. A 182 (1999) 257.
[60] D. Vidick, M. Herlitschke, C. Poleunis, A. Delcorte, R.P. Hermann, M. Devillers, S. Hermans, J. Mater. Chem. A 1 (2013) 2050–2063.
[61] S. Hermans, C. Diverchy, V. Dubois, M. Devillers, Appl. Catal. A: Gen. (2013), http://dx.doi.org/10.1016/j.apcata.2013.09.029 (in press).
[62] P. Chini, L. Colli, M. Peraldo, Gazz. Chim. Ital. 90 (1960) 1005.
[63] J.N. Nicholls, M.D. Vargas, J. Hriljac, M. Sailor, Inorg. Synth. 26 (1989) 280.
[64] S. Hermans, T. Khimyak, B.F.G. Johnson, J. Chem. Soc. Dalton Trans. (2001) 3295.
[65] M.I. Bruce, E. Horn, P.A. Humphrey, E.R.T. Tiekink, J. Organomet. Chem. 518 (1996) 121.
[66] B.F.G. Johnson, J. Lewis, W.J.H. Nelson, J.N. Nicholls, J. Puga, P.R. Raithby, M.J. Rosales, M. Schröder, M.D. Vargas, J. Chem. Soc. Dalton Trans. (1983) 2447.
[67] A.G. Cowie, B.F.G. Johnson, J. Lewis, P.R. Raithby, J. Chem. Soc. Chem. Commun. (1984) 1710.
[68] T. Khimyak, B.F.G. Johnson, S. Hermans, A.D. Bond, Dalton Trans. (2003) 2651.
[69] C. Willocq, D. Vidick, B. Tinant, A. Delcorte, P. Bertrand, M. Devillers, S. Hermans, Eur. J. Inorg. Chem. (2011) 4721–4729.
[70] P.A. Bazula, A.H. Lu, J.J. Nitz, F. Schuth, Micropor. Mesopor. Mater. 108 (2008) 266.
[71] S. Kundu, Y.M. Wang, W. Xia, M. Muhler, J. Phys. Chem. C 112 (2008) 16869.
[72] H. Darmstadt, C. Roy, S. Kaliaguine, S.J. Choi, R. Ryoo, Carbon 40 (2002) 2673.
[73] M.L. Toebes, E.M.P. van Heeswijk, J.H. Bitter, A.J. Dillen, K.P. de Jong, Carbon 42 (2004) 307.
[74] U. Dettlaff-Weglikowska, V. Skakalova, R. Graupner, S.H. Jhang, B.H. Kim, H.J. Lee, L. Ley, Y.W. Park, S. Berber, D. Tomanek, S. Roth, J. Am. Chem. Soc. 127 (2005) 5125.
[75] J.K. Wassei, K.C. Cha, V.C. Tung, Y. Yang, R.B. Kaner, J. Mater. Chem. 21 (2011) 3391.
[76] C. Laslau, W. Henderson, Z.D. Zujovic, J. Travas-Sejdic, Synth. Met. 160 (2010) 1173.
[77] S. Hermans, T. Khimyak, N. Feeder, S.J. Teat, B.F.G. Johnson, Dalton Trans. 4 (2003) 672–684.